Complementary cathodoluminescence lifetime imaging configurations in a scanning electron microscope

S. Meuret[1], M. Solà Garcia[1], T. Coenen[1,2], E. Kieft[3], H. Zeijlemaker[1], M. Lätzel[4], S. Christiansen[4], S.Y. Woo[5], Y-H Ra[6], Z. Mi[7] and A. Polman[1]

[1]Center for Nanophotonics, AMOLF
Science Park 104, 1098 XG Amsterdam, the Netherlands

[2]Delmic BV
Kanaalweg 4, 2628 EB Delft, the Netherlands

[3]Thermo Fisher Scientific
Achtseweg Noord 5, 5651 GG, Eindhoven, the Netherlands

[4]Max Planck Institute for the Science of Light,
Staudtstrasse 2, 91058 Erlangen, Germany

[5] Department of Materials Science and Engineering, Canadian Centre for Electron Microscopy, McMaster University, 1280 Main Street West, Hamilton, Ontario L8S 4M1, Canada

[6] Department of Electrical and Computer Engineering, McGill University,
3480 University Street, Montreal, Quebec H3A 0E9, Canada

[7] Department of Electrical Engineering and Computer Science, University of Michigan, Ann Arbor, MI 48109, USA

Abstract

Cathodoluminescence (CL) spectroscopy provides a powerful way to characterize optical properties of materials with deep-subwavelength spatial resolution. While CL imaging to obtain optical spectra is a well-developed technology, imaging CL lifetimes with nanoscale resolution has only been explored in a few studies. In this paper we compare three different time-resolved CL techniques and compare their characteristics. Two configurations are based on the acquisition of CL decay traces using a pulsed electron beam that is generated either with an ultra-fast beam blanker, which is placed in the electron column, or by photoemission from a laser-driven electron cathode. The third configuration uses measurements of the autocorrelation function $g^{(2)}$ of the CL signal using either a continuous or a pulsed electron beam. The three techniques are compared in terms of complexity of implementation, spatial and temporal resolution, and measurement accuracy as a function of electron dose. A single sample of InGaN/GaN quantum wells is investigated to enable a direct comparison of lifetime measurement characteristics of the three techniques. The $g^{(2)}$-based method provides decay measurements at the best spatial resolution, as it leaves the electron column configuration unaffected. The pulsed-beam methods provide better detail on the temporal excitation and decay dynamics. The ultra-fast blanker configuration delivers electron pulses as short as 30 ps at 5 keV and 250 ps at 30 keV. The repetition rate can be chosen arbitrarily up to 80 MHz and requires a conjugate plane geometry in the electron column that reduces the spatial resolution in our microscope. The photoemission configuration, pumped with 250-fs 257-nm pulses at a repetition rate from 10 kHz to 25 MHz, allows creation of electron pulses down to a few ps, with some loss in spatial resolution.

1 Introduction

The design and optimization of optical materials and devices often requires analysis of optical characteristics at length scales below the optical diffraction limit. Cathodoluminescence spectroscopy (CL) is a well-known nanoscale characterization technique in which a high-energy electron beam is scanned over a sample and the emitted light is collected [1]. CL generates two-dimensional optical excitation images with a spatial resolution down to 10 nm, far below the optical diffraction limit. In conventional CL spectroscopy, optical spectra are collected and analyzed. However, in many cases it is essential to have information on the dynamics of the electron-beam induced optical excitation processes. To that end, time-resolved cathodoluminescence (TR-CL), using either pulsed [2]–[4] or continuous electron beams [5][6], has been introduced.

The first realization of TR-CL in an electron microscope used a pulsed excitation scheme in which the continuous electron beam was swept over an aperture. Using long pulses (100 ns) with relatively sharp falling pulse edge (< 1 ns), Bell et al. [7] and others [8] achieved sub-nanosecond time resolution. This was used to study the quantum-confined Stark effect in single InGaN quantum wells, for example. However, the sweep over the aperture led to a significant loss in spatial resolution (a few micrometers), making it impractical for nanoscale time-resolved experiments. The first time-resolved cathodoluminescence scheme reaching picosecond electron pulses and 50 nanometer spatial resolution was demonstrated by Merano et al. [2]. In that case a gold photocathode in a scanning electron microscope (SEM) was driven by a pulsed laser. In order to improve the coherence and the energy spread a field emission electron gun instead of a gold cathode was used by the group of Zewail [9], [10]. A laser-driven field emission gun (FEG) source was implemented later in a transmission electron microscope (TEM) by the group of Ropers [11], taking advantage of the higher coherence offered by the FEG [12]. Time-resolved spectroscopy based on a laser-driven electron gun was developed in parallel in different groups, including for example the work by Chichibu et al. in which TR-CL and time-resolved photoluminescence (PL) were acquired within the same experiment [13]. This laser-driven cathode configuration used very short pulses and therefore the excited sample does not reach the steady state within the pulse and allowed to achieve better time resolution. Later, in subsequent developments, ultrafast pulses (90 ps) were obtained with an ultrafast blanker configuration while maintaining a spatial resolution of 50 nm using conjugate blanking [4]. More recently, it was shown that time-resolved decay statistics could also be derived from autocorrelation measurements of CL generated by either continuous [5] or pulsed electron beams [14].

Each of the TR-CL techniques enable the determination of the CL lifetime and are characterized by differences in complexity of the experimental setup, spatial resolution, time resolution, optical detection scheme, and signal-to-noise ratio. In this paper we present a systematic comparison of lifetime measurements in cathodoluminescence using 1) an ultrafast blanker, 2) photoemission, and 3) the autocorrelation function, and compare their advantages and disadvantages. In our analysis, we use a GaN substrate with 10 embedded InGaN quantum wells (QWs) to carry out TR-CL using each of three techniques, enabling a direct systematic comparison between them.

2 Technical design and realization of three TR-CL techniques

2.1 Ultrafast beam blanker

In this geometry a set of electrostatic deflection plates (spacing L = 0.25 - 2 mm) is incorporated inside the electron column of a Thermo Fisher Scientific/FEI Quanta 650 SEM equipped with a

thermionic FEG (see Fig. 1). The plates are driven by an electronic shape generator that delivers a square positive-negative (e.g. ±5 V) voltage to the blanking plate. To simultaneously achieve high temporal and spatial resolution, the electron beam cross-over is placed at the center between the blanking plates [15]. This conjugate blanking condition is achieved by lowering the current of the condenser lens C2 (see Fig. 1). In the optimized settings image distortion is minimized while blanking. As in continuous mode, the optimal C2 voltage changes with acceleration voltage and current. To minimize the electron pulse width, an aperture of 70 μm is placed at the low-pressure aperture (LPA) position below the pole piece (see Fig. 1). To optimize the effect of the beam sweep, the angular distribution in the beam was restricted by reducing the top aperture placed after condenser lens C2 from 400 μm to 30 μm. The combination of the two apertures decreases the electron pulse duration on the sample by a factor 20.

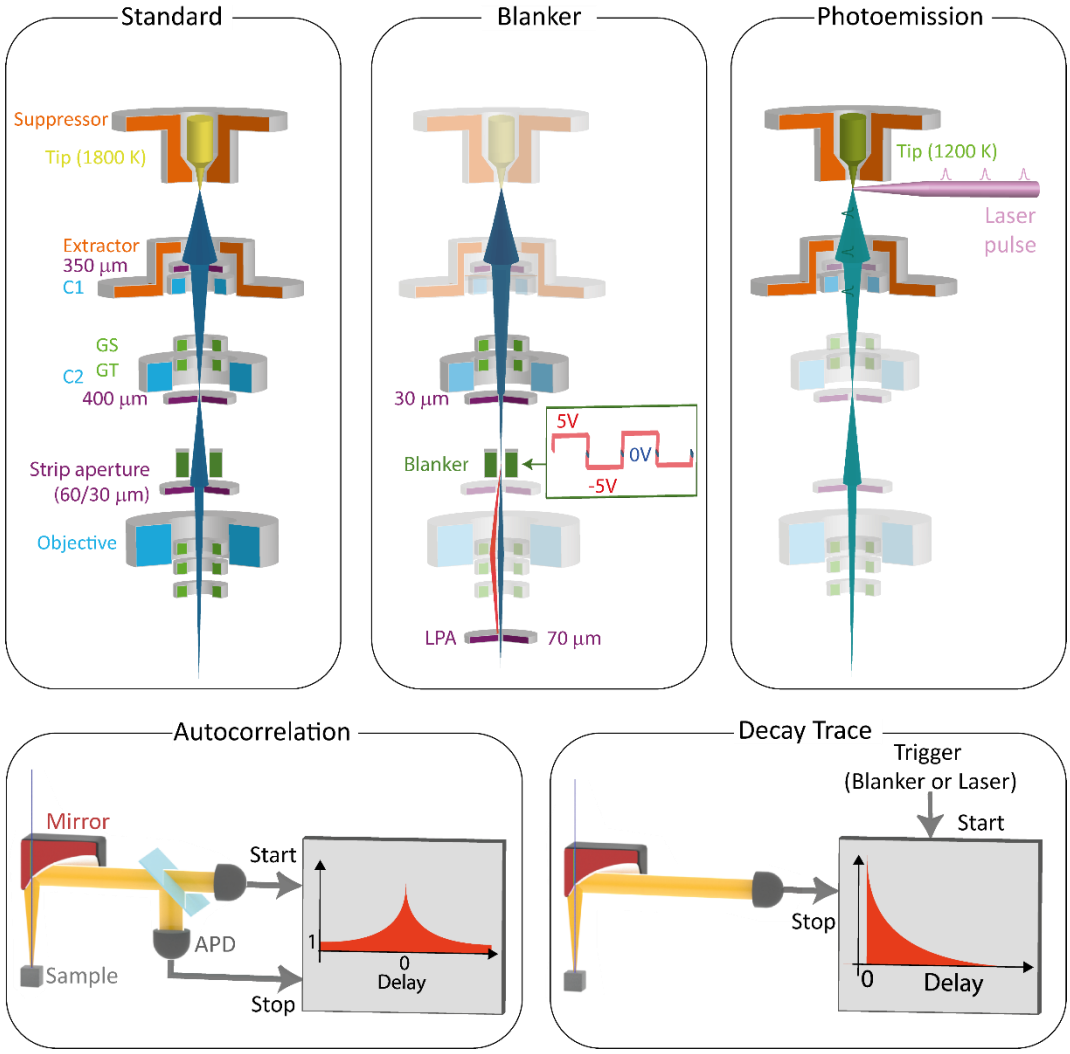

Figure 1: Schematics of the different configurations of the TR-CL microscopes. Column configurations; left: standard SEM column (GT: gun tilt, GS: gun shift); center: ultrafast electrostatic blanker configuration, right: pulsed-laser driven configuration. Components that are not changed compared to the standard configuration are faded. Time-resolved detection schemes: left: in autocorrelation mode the light collected by the parabolic mirror is sent to a Hanbury Brown and Twiss intensity interferometer where a histogram of the delay between detected photons is recorded; right: in the decay trace mode light is sent to a detector and a histogram of the time between a trigger signal and CL detection is recorded.

By replacing the top aperture, the electron current in normal (non-conjugate) imaging mode is not affected. However, the microscope column becomes more sensitive to beam misalignment and requires a more elaborate mechanical alignment procedure and control of gun lenses. Using the geometry described here an electron pulse duration on the sample below 30 ps is achieved at 5 keV, as will be shown below. Alternative approaches for restricting the beam angular distribution can be envisioned, for example by using an optimally sized electron beam aperture in a different place in the microscope column. Such a set-up would be less sensitive to column misalignment thus providing improved long-term stability with identical performance in the time and space domains. A major advantage of using an electrostatic beam blanker compared to the laser-driven cathode configuration used for most pulsed electron beam experiments [2], [12], [16] is the ease with which the microscope can be switched from a pulsed to continuous electron beam, which can be achieved by only switching on and off the blanker driving signal. Additionally, the repetition rate of the electron beam can be modified more easily than in the laser-driven system.

2.2 Ultrafast laser driven photocathode

A second technique to obtain a pulsed electron beam is by driving the field emission gun tip with femtosecond laser pulses (see Fig. 1). In this case the electron pulses are created directly at the electron cathode by photoemission. This process has been used before to obtain pulsed electron beams for time-resolved SEM/TEM studies [2], [11], [12], [17]. We use a Schottky FEG (tungsten cathode coated with zirconium oxide). In this case the pulsed electron beam is created directly at the FEG cathode by photoemission. Other regimes of laser-driven electron emission have also been reported, such as optical field emission, but the latter requires a stronger and more localized electric field on the tip than used in our experiments [18], [19].

The experiments are performed on a Thermo Fisher Scientific/FEI XL30 SEM, which is equipped with a UV-transparent vacuum window in the tip assembly. In order to obtain a pulsed electron beam, the continuous thermionic emission is fully suppressed by reducing the filament current by 32% with respect to normal operation, thus lowering the temperature of the tip from the normal continuous operating temperature of 1800 K to approximately 1200 K. In order to increase the collection of photoemitted electrons the extractor voltage can be decreased from the usual 4247 V to 747 V. We have observed that the reduced voltage leads to a higher collected current in pulsed conditions, but at the expense of lower spatial resolution, as will be discussed in Section 3.2. The C1 condenser (see Fig. 1) voltage settings were readjusted depending on the extractor configuration. Changing the tip temperature takes time and makes it less straightforward to switch from pulsed to continuous mode compared to the electrostatic blanking described in Section 2.1.

We use an Yb-doped fiber femtosecond laser (Clark MXR) with pulse width of approximately 250 fs, output wavelength of 1030 nm, repetition rate ranging from 10 kHz to 25 MHz and maximum pulse energy of 10 μJ. We do not select a specific polarization, even though it is known to have some effect on the photoemission efficiency [10]. The laser beam is sent through a harmonic generator to obtain the 2^{nd} (515 nm), 3^{rd} (343 nm), and 4^{th} (257 nm) harmonics of the primary beam. We use either the 3^{rd} or 4^{th} harmonic to excite the FEG tip, given that in both cases the photon energy exceeds the photoemission energy threshold for Zr/O-coated W (~2.9 eV) [12].

2.3 Decay trace acquisition

2.3.1 Ultrafast beam blanker

The CL is collected using a Delmic SPARC CL detection and analysis system, and focused onto a 100-μm-diameter multimode optical fiber that guides the light to an optical breadboard. The latter contains focusing optics to couple the light into an avalanche photodiode (APD), from MPD (PD-100) (see Fig. 1 for schematic overview). In the beam path there is room to place bandpass and/or neutral density filters. A Picoquant PicoHarp300 correlator records the photon counts and builds a delay histogram, using the beam blanker driving signal as a trigger. In this way a CL decay trace is built up over time.

2.3.2 Ultrafast laser driven photocathode

Lifetime measurements are performed using the same detection scheme and components (APD and correlator) as in the ultrafast blanker configuration described above. This allows for an accurate comparison between the two types of experiments, despite intrinsic differences due to the fact that we use two different microscopes. In the laser-driven configuration the correlator is triggered by a photodiode, which detects the 3^{rd} harmonic of the laser. The parabolic mirror light collection geometry in the SEM chamber is identical in the two setups.

2.4 Photon correlation measurements

In this configuration, it is not required to pulse the electron beam to obtain time-resolved information because it relies solely on the light detection scheme. We use the same Quanta SEM used in the blanker configuration (section 2.1) but operate it in the conventional configuration, with a continuous electron source which is known to have Poissonian electron emission statistics [20]. The light emitted by the sample is collected by the CL system as described in Section 2.1, and sent to a Hanbury Brown and Twiss (HBT) intensity interferometer equipped with two APDs (see Fig. 1) [21]. The HBT interferometer measures the delay between two photons detected by the APDs. A time delay histogram is built, counting the number of events recorded with a certain delay τ between two recorded photons. This histogram is then normalized by the average number of events recorded per time bin at long delay, which corresponds to the Poissonian statistics of an uncorrelated electron beam [14], leading to the autocorrelation function, $g^{(2)}(\tau)$.

The HBT geometry has been used extensively in optical measurements to determine the quantum nature of single emitters ($g^{(2)}(0) < 1$)[22], [23], to identify the lasing threshold ($g^{(2)}(0) = 1$)[24], or to observe the formation of Bose-Einstein condensates ($g^{(2)}(0) = 2$)[25]. In CL spectroscopy, it has been found that a single electron can create multiple excitations, resulting in the emission of photon bunches (in the case of a non-single-photon emitter) so that $g^{(2)}$ can be much larger than unity ($g^{(2)}(0) >> 1$) [26]. The amplitude of the $g^{(2)}(0)$ peak is determined by the electron beam current [26], the excitation probability [14], and the lifetime of the emitter [5]. This lifetime can be retrieved by an exponential fit of the $g^{(2)}(\tau)$ curve around $\tau = 0$. In this paper we have performed these $g^{(2)}$ measurements on the Quanta SEM in continuous mode.

$g^{(2)}$ can also be measured under pulsed conditions as was demonstrated in Ref. [14]. In that case, the main bunching peak is observed around $\tau = 0$, and smaller peaks are observed at periodic intervals determined by the frequency of the blanker driving signal. The peak at $\tau = 0$ represents the statistics of photons created within the same electron pulse, whereas the other peaks represent the correlation of photons generated by different pulses [14]. Here too, the emitter lifetime can be

retrieved by an exponential fit of the $g^{(2)}(\tau)$ curve around $\tau = 0$. Pulsed $g^{(2)}$ measurements can be used to increase the signal-to-noise ratio, as is the case in optics [27]. Moreover, they provide an effective method to study single-electron effects on the light emission.

3 Spatial resolution

In order to compare the spatial resolution (η) in the different configurations we acquired SEM images on a carbon substrate covered with quasi-spherical tin particles, as often used for SEM calibration and alignment. The tin particles have different diameters ranging from 10 nm to a few microns and are randomly distributed on the sample. They produce a large number of secondary electrons per incident electron and provide a strong contrast with the underlying substrate, making them ideal for characterizing the SEM performance at low beam currents. The images shown here are recorded without the parabolic mirror used for the CL experiments so that the sample could be placed at the optimum height (10 mm for the Quanta and 5.5 mm for the XL30) to obtain the highest spatial resolution. This allows us to compare images from the two microscopes, which would be difficult with the CL mirror in place because the mirror in the XL30 strongly reduces the signal of the secondary electron detector, therefore lowering the signal-to-noise ratio of the image. In contrast, on the Quanta the position of the secondary electron detector was optimized to more efficiently collect secondary electrons when the mirror is placed. Several methods exist to assess spatial resolution in SEMs, each with their own advantages and disadvantages. We use a power spectrum-based technique as outlined in ref. [28]. More details about the procedure are given in appendix A. Figure 2 shows a selection of representative images for the different configurations discussed in this paper.

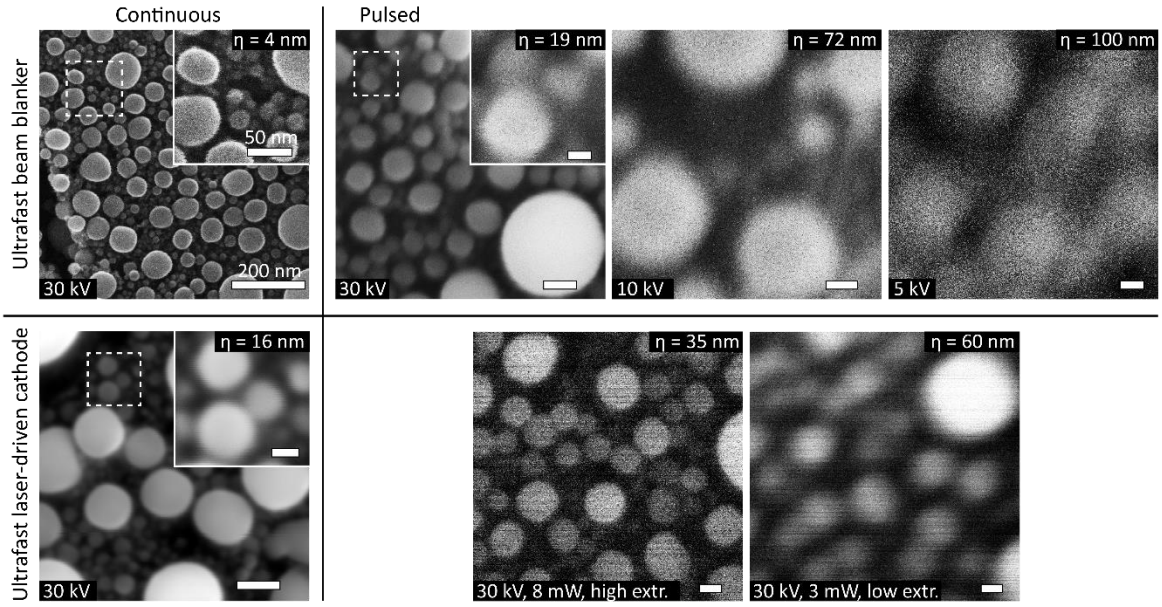

Figure 2: SEM images for the electrostatically blanked Quanta (top row) and laser driven XL-30 (bottom row). For some images the areas indicated by the white dashed squares are enlarged and shown as an inset to better show how small features are resolved at those conditions. Top row shows from left to right: 30 keV continuous beam under normal conditions, conjugate blanking mode using L = 0.25 mm and 10 V blanking voltage for 30 keV, 10 keV, and 5 keV. Bottom row: 30 keV continuous beam under normal conditions; 30 keV pulsed (λ = 257 nm, 8 mW), and extractor at 4247 V; 30 keV pulsed (λ = 257 nm,3 mW) with extractor at 747 V. Both pulsed images were acquired with a repetition rate of 25.2 MHz. The retrieved spatial resolution

is shown on the top-left corner of each image. The scale bars in the images are 200 nm and 50 nm for the insets.

It is important to note that the changes in spatial resolution discussed here are connected to changes in the width of the electron beam. Therefore, the resolutions found present an upper limit to the spatial resolution that can be reached in CL. For CL the final spatial resolution will depend on the material (carrier diffusion, mean free path...), the thickness and the electron beam energy, which together define the interaction volume in which CL is generated [29]. This aspect is not solely connected to time-resolved configurations but should always be considered in CL analyses.

3.1 Ultrafast beam blanker

In the case of a pulsed electron beam driven by a fast blanker the beam is continuously swept across the LPA aperture. In theory, when the beam cross-over is between the blanking plates, the blanker and sample are in conjugate planes, meaning that the electron probe should stay steady on the sample even if the electron beam is swept, only disappearing if the electron beam is blocked by the LPA aperture. Therefore, in theory the spatial resolution should be the same in continuous and in pulsed modes. However, several factors affect the resolution.

First, in the conjugate blanking configuration the voltage of the C2 condenser is reduced by ~50% to lower the cross-over to a position between the blanking plates (see Figure 1). This reduces the effect of the low aperture (a strip of 6 round apertures of different sizes) on beam definition, which decreases the spatial resolution by a factor 2. Moreover, the addition of the 70 μm LPA at the bottom of the pole piece adds some aberrations reducing the resolution by another factor of 1.5. Because of these factors the spatial resolution in continuous mode at 30 keV degrades from ≈4 nm to ≈12 nm at 30 keV (see Fig. 2).

Second, a precise centering of the cross-over between the blanking plates is crucial to obtain a sharp symmetric beam profile. Ideally, the tip, the 30 μm aperture, the center of the blanking plate and the 70 μm aperture should be aligned with a precision better than 10 μm. In practice this cannot be achieved and the trajectory of the beam is corrected with the gun coils, leading to an increase of the astigmatism.

Third, the electric field profile between the blanking plates (determined by blanker voltage and spacing between the plates L) also affects the electron beam profile, reducing the spatial resolution further. Altogether, the factors described above lead to deterioration of the spatial resolution from η = 4 nm for a continuous beam to η = 19 nm for the blanked beam at 30 keV (see Fig. 2). Reducing the electron energy reduces the resolution further: η = 72 nm at 10 keV, η = 100 nm at 5 keV, all using the same blanker plate distance L = 0.25 mm. As will be shown below, using a lower beam energy results in a much higher temporal resolution of the electron pulse. Both the loss in spatial resolution and increase in time resolution, at lower voltage, are due to a faster sweep of the electron beam over the aperture. In particular, the electron beam is more susceptible to aberrations that are induced by the blanker configuration. We note that the use of a pulsed beam obviously reduces the effective beam current drastically, reducing the signal-to-noise ratio of the secondary electron images.

3.2 Ultrafast laser-driven photocathode

In the geometry of the laser-driven cathode, we drastically change the way electrons are emitted from the tip with respect to the continuous beam configuration. However, in principle the settings of the electron column itself can be kept the same as in continuous mode, which implies that fundamentally a similar spatial resolution can be achieved. Indeed, several reports have shown spatial resolutions down to 5 nm in a pulsed-laser driven SEM [17] and a resolution of 0.9 nm in TEM, in which a new laser driven cathode system using a cold-FEG was demonstrated [19]. In our case, the spatial resolution is partially limited by the intrinsic limitations of the XL30 SEM, which has a resolution of 16 nm in continuous mode. Nevertheless, we will discuss parameters that can affect the spatial resolution in the laser-driven cathode configuration with respect to the continuous mode.

Increasing the laser power leads to a higher average number of electrons generated per pulse. If multiple electrons are created per pulse, temporal and spatial broadening can be observed due to Coulomb repulsion, analogous to the well-known Boersch effect [12], [30]–[32], in which the energy spread of a charged particle beam increases due to Coulomb repulsion. In our case the laser spot size on the tip is $10 - 15$ μm, which is limited by the numerical aperture of the illumination. Reducing the spot size would lead to a smaller photoemission region on the tip, resulting in a higher brightness and spatial resolution [17], [19]. Aside from the excitation conditions of the tip, several column settings determine the spatial resolution. At the extractor voltage that is used in continuous mode (4247 V) the highest spatial resolution is achieved, but at the expense of a low average current on the sample (less than 6 pA for a laser power at λ = 257 nm of 58 mW at 25.2 MHz). This is because the large difference between suppressor (-500 V, same as in continuous mode) and extractor voltages blocks a large part of the electron beam emitted from the cathode by the 350-μm-diameter extractor aperture. In other words, lowering the extractor voltage selects a larger fraction of the emission current, leading to a larger effective source size and loss in resolution. Using the high-extractor configuration, as in continuous conditions, the spatial resolution was found to be η=35 nm at a beam current of 1.4 pA (λ = 257 nm, 8 mW, 25.2 MHz, 30 μm objective aperture), as seen in Fig. 2. In the images in Fig. 2 corresponding to the laser driven cathode system, some dark lines are visible, which correspond to fluctuations in the laser intensity and coupling efficiency between the laser and the cathode.

Using an extractor voltage of 747 V allows for a higher current but a reduced spatial resolution. At a beam current on the sample of 11 pA (λ = 257 nm, 3 mW, 30 μm aperture) the spatial resolution is 60 nm (Fig. 2). Lowering the extractor voltage results in a change of the cross-over position inside the column. Therefore, the condenser voltage C1 needs to be readjusted in order to place the cross-over in the corresponding plane. In the image shown in Fig. 2, the optimum C1 was found to be 560 V, in contrast with 1159 V used in normal continuous conditions.

4 Time resolution

Next, we compare lifetime measurements performed using the three TR-CL techniques. We consider both the time resolution and the accuracy of the different measurements. We first discuss the limits in time resolution.

4.1 Ultrafast beam blanker

For the electrostatic beam blanker configuration, the instrument response function (IRF) is determined by three different time error sources: (1) the electron pulse width (between 30 ps and 2 ns, depending on the configuration), (2) the combined APD timing jitter and precision of the

correlator (~ 46 ps, see below), and (3) the time precision of the electronic trigger. In addition, for spectrally broadband signals, dispersion of light in the multi-mode fiber that guides the light to the APD creates further time variation, which could be eliminated by having a fully-free-space coupled optical detection system.

The electron pulse width is determined by the time needed for the beam to be deflected beyond the aperture cut-off angle α_c which is determined by the LPA radius and the distance between the aperture and the center of the blanker plates. The electrostatic beam deflection angle α is described by:

$$\tan(\alpha) = 0.5\left(\frac{H}{L}\right)\left(\frac{qV}{E}\right) \qquad (1)$$

where H is the length of the blanking plates (here 6.5 mm), L the separation between the plates, V the voltage across the plates and E the electron energy. The temporal width of the electron pulse is then determined by the time needed for the voltage to reach the value to deflect the beam by α_c. This time is determined by the steepness of the slope of the square voltage pulse on the blanker plates, which depends on the frequency response of the pulse generator and the RC time of the blanker. In our analysis we compare measurements of the average beam current in pulsed and continuous configurations and derive the electron pulse width Δ_p from:

$$\Delta_p = \frac{I_p}{F I_c} \qquad (2)$$

with I_c and I_p the current in continuous and in pulsed modes, respectively and F the blanking frequency. This measurement gives an estimate of the pulse width but is less precise than a direct measurement of the electron pulse width with a streak camera, as implemented by Moerland et al. [4]. Our method also assumes a negligible temporal spread of the pulse between the blanking aperture (LPA at the end of the objective lens) and the sample. In Figure 3a we plot Δ_p as a function of frequency F for beam energies of 5, 10, and 30 keV and different voltage amplitudes of the squared input signal, with L = 0.25 mm in all cases. Several trends can be observed. For a 30 keV electron beam at frequencies below 50 MHz, the pulse width decreases from Δ_p = 900 ±75 ps to Δ_p = 250 ± 40 ps as the voltage is increased from 3 to 10 V, consistent with the fact that the beam is swept faster across the LPA aperture. Furthermore, Figure 3a shows that the pulse width decreases as the beam energy decreases, consistent with the larger beam deviation across the aperture (Eqn. 1): at a voltage V = ±5 V at frequencies in the range 20-50 MHz we find Δ_p = 80 ± 20 ps for 10 keV and Δ_p = 30 ± 6 ps for 5 keV. For 30 keV electrons we observe a decrease in beam pulse width as the blanker frequency is increased. This is attributed to a faster rise time of the input signal (square ±5 V) when the repetition rate is above 50 MHz (300 ps/V instead of 500 ps/V).

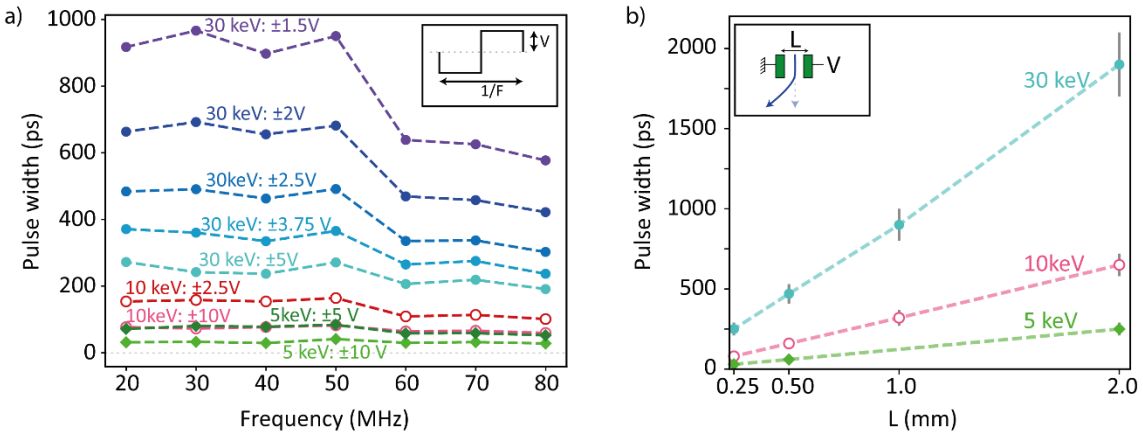

Figure 3: Electron beam pulse width for the ultrafast beam blanker configuration derived from current measurements in pulsed and continuous modes. a) Pulse width as function of blanker frequency for different amplitudes (V) of the square driving signal and an electron energy of 5, 10, and 30 keV, with L=0.25 b) Pulse width as function of distance (L) between the blanking plates, for 5, 10, and 30 keV electron beams.

Figure 3b shows the effect of varying the distance L between the blanking plates on the pulse width for electron energies of 5, 10, and 30 keV at a blanker voltage of ±5 V. We plot the average pulse width measured at 20, 30, 40 and 50 MHz, with the error bar representing the minimum and the maximum measured values. The pulse width increases linearly with L in agreement with the fact that the field strength is inversely proportional to L. The shortest pulse width observed is $\Delta p = 30 \pm 6$ ps, which is reached for 5 keV, V = ±5 V and L = 0.25 mm. One of the advantages of the ultrafast blanking configuration compared to photoemission configuration is the flexibility to adjust the blanking conditions for a particular experiment over a wide range of repetition rates and pulse widths, with the corresponding spatial resolutions, as shown in Figure 2 and Figure 3.

In order to experimentally determine the total time response of the system, we measured the time response of transition radiation at $\lambda = 500 \pm 20$ nm excited on a single-crystalline gold sample at 30 keV. Transition radiation is emitted in the form of femtosecond wave packets with a duration of less than 20 fs [33]. Hence, we can consider that photon emission upon excitation is effectively instantaneous compared to the time resolution of the system. The measured time response should therefore represent the overall time response of the system. Figure 4 shows the system response for the four different blanker spacings L (at V=±5 V), taken with a repetition rate of 8 MHz. As L decreases from 2 to 1 mm, the IRF width, derived from Gaussian fits to the data, decreases from 2.1 ns to 1.1 ns full-width-at-half-maximum (FWHM). These results agree with the pulse width found by measuring the current (see Fig. 3b), indicating that the electron pulse width is limiting the time resolution for these settings. For L = 0.5 mm and L = 0.25 mm the FWHM of the time traces is 585 ± 10 ps and 350 ± 7 ps respectively, significantly larger than the electron pulse widths found in Fig. 3b ($\Delta_p = 470 \pm 60$ ps; $\Delta_p = 250 \pm 40$ ps, respectively). The difference corresponds to an additional system error of 350 ± 110 ps and 270 ± 40 ps for L = 0.5 and 0.25 mm, respectively. This is mostly explained by the timing error of the electronic trigger, even after synchronization of the internal clocks of the shape generator and the delay generator (see Fig. 4c). We measured a timing error of about 270 ps at 8 MHz. The time response of the detection path was measured separately by sending a $\lambda = 515$ nm 250-fs laser pulses both on the photodiode (50 ps) and the APD (46 ps). It was found to be 70 ps FWHM (see Fig. 4a). We conclude that while the electron pulses in the blanker configuration can be made as short as 30 ps at 5 keV, the time-resolved measurements presented in Figure 4

configuration are limited by the time jitter in the electronics, mainly originating from the triggering of the delay generator by the shape generator (see Fig 4c).

This trigger jitter can be eliminated by using only the delay generator, without the shape generator, (see Fig. 5b) to produce both the square signal that drives the blanking plates and the NIM signal for the correlator. Furthermore, the rise time of the square signal is shorter (0.3 ns/V) than in the case of the shape generator (0.5 ns/V). The pulse width is therefore also reduced in this configuration and we found, for L=0.25 mm and V = ±2V, Δ_p= 165 ps and Δ_p=46 ps at 30 keV and 10 keV, respectively. A drawback of this configuration is that it is less flexible in terms of voltage amplitude (max. 5V) and repetition rate (max. 4 MHz). As a confirmation we also measured the IRF for these two configurations using transition radiation with the same color filter. The results are shown in Fig. 5. In these conditions, the FWHM of the IRF measured for 30 keV and 10 keV is 259 ps and 141 ps, respectively. The reduction of the IRF FWHM is both due to reduction of the electrical trigger jitter as well as a shorter pulse length.

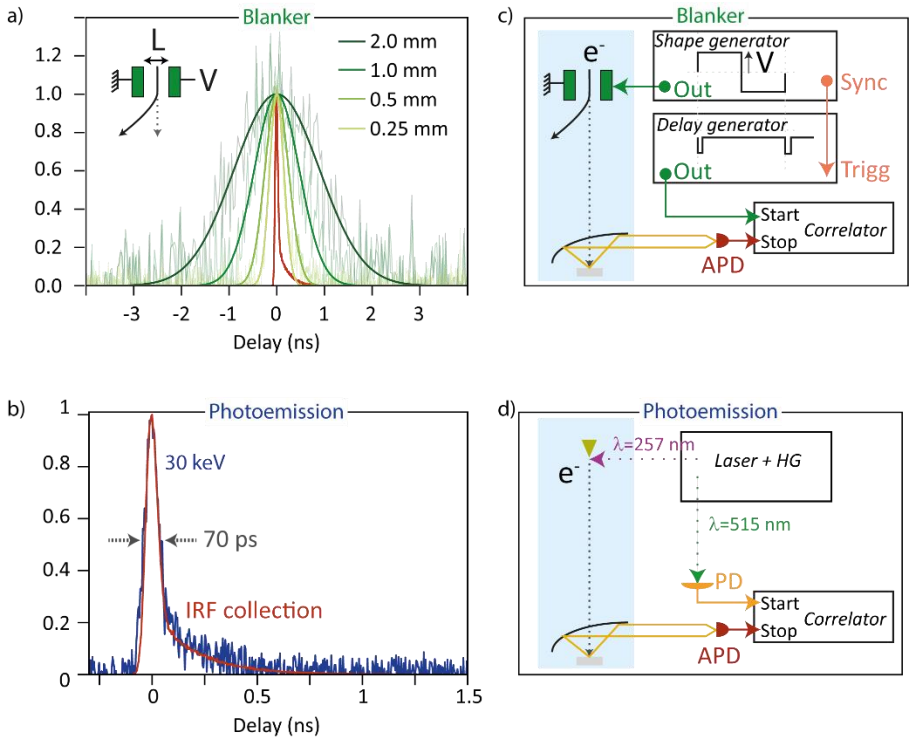

Figure 4: Instrument response function (IRF) measured using transition radiation from Au at 30 keV. a) CL signal at 500 nm for the 4 blanker spacings (green curves, 8 MHz, ±5V). The drawn curves are Gaussian fits. The IRF of the APD/correlator/photodiode detection system (red) is measured using λ = 515 nm 250-fs laser pulses at 25.19 MHz. b) CL signal at 500 nm for the photoemission configuration (blue), and IRF of the APD/correlator/photodiode detection system (red, same as in a). c) Sketch of the trigger line for the blanker configuration, the square signal produced by the shape generator and the collection of the CL signal by the APD. d) Sketch of the trigger line from the laser that triggers the photodiode (PD) and the CL signal that triggers the APD.

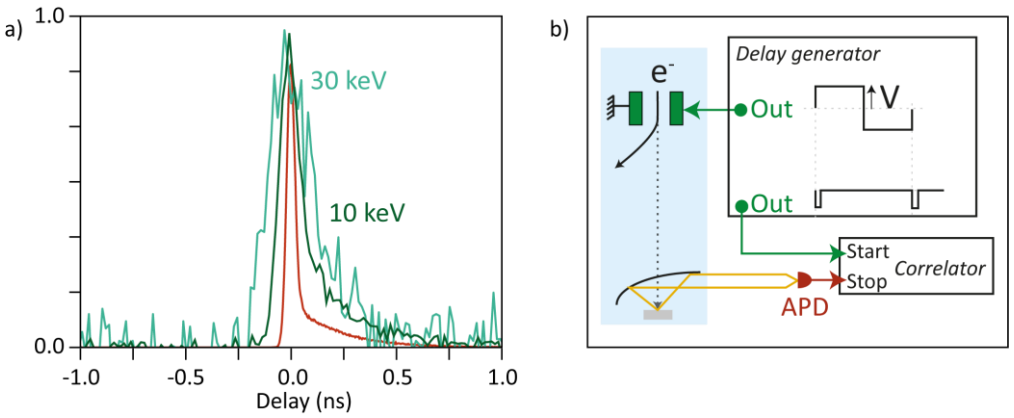

Figure 5 : a) Instrument response function (IRF) measured using transition radiation from Au (green lines) at 30 keV and 10 keV for L=0.25 mm and V = ± 2V. The IRF of the collection system is shown for comparison (red line). b) Sketch of the trigger line, the delay generator is now producing both the squared signal for the blanking plate and the trigger signal for the correlator.

4.2 Ultrafast laser-driven photocathode

One of the major advantages of the laser-driven photocathode configuration compared to the ultrafast beam blanker is that it enables the generation of even shorter (~1 ps) electron pulses. The measurement of such short pulses requires sub-picosecond resolution light detection with e.g. streak camera, direct time-resolved detection of the electrons arriving at the sample [4], or a pump-probe experiment in which the variation in for example secondary electron contrast is measured [34]. Here, we measure transition radiation from Au, as above, under pulsed excitation. The time trace is plotted in Fig. 4b and has a width of 70 ps FWHM. The IRF is very similar to the IRF of the detection path described in section 4.1, which is plotted again in Fig. 4b. The fact that the temporal resolution is only limited by the detection system implies it can be further improved by using a faster APD or a streak camera [2], [35].

4.3 Photon correlation measurements

In the case of a $g^{(2)}$ measurement in continuous mode the lifetime is determined by analyzing the statistics of the detection of photons generated by the same electron. Therefore, there is no uncertainty in the time of excitation and the only parameters that influence the time resolution are linked to the detection scheme. For $g^{(2)}$ measurements two APDs are used (Figure 1), and therefore the time resolution of the experiment is only determined by the resolution of the APDs and the correlator. We evaluated the time resolution to be 70 ps, mainly determined by the resolution of the two APDs (46 ps per APD). In the case of pulsed $g^{(2)}$, if the average number of electrons per pulse is smaller than 1, the $g^{(2)}$ peak at 0 delay is only limited by the detection scheme and not by the pulse width, as the measured photons are generated by the same electron [14].

5 Lifetime measurement and accuracy

To determine the CL lifetime we acquire either a decay trace, in the case of pulsed excitation (ultrafast blanker and laser-driven cathode) or the autocorrelation function, in the case of $g^{(2)}$ measurements (continuous or pulsed). The model to retrieve the lifetime from the data is therefore different for the two acquisition modes. In this section we discuss the detection schemes, and

compare them in terms of electron dose, signal-to-noise ratio, and accuracy for lifetime determination.

5.1 Collecting the data

In both excitation configurations a time-delay histogram is built up. In the case of the acquisition of a decay trace, the measurement speed is limited by the pile-up effect that occurs if on average more than one photon reaches the detector per electron pulse [36]. This effect, well known in time-resolved photoluminescence, can be amplified in CL measurements by the fact that a single electron can generate a bunch of photons [26]. Therefore, a neutral density filter is used to control the photon count rate. The acquisition time for a single decay trace typically is ~30 s for a bright sample such as the InGaN/GaN heterostructure investigated here. From the measured decay trace the lifetime is obtained by fitting with either a single-, multi-, or stretched-exponential model convolved with a Gaussian, which represents the IRF, as discussed in Section 4.

In the case of the acquisition of the $g^{(2)}$, the pile-up effect is less likely to play a role as two detectors are used rather than one. The data are fitted with the same decay function as the decay trace, but without the need to convolve with the IRF as the curve is symmetric around 0 delay.

The sample used in this comparison is a bright LED sample, consisting of ten 2-nm-thick InGaN quantum wells embedded in GaN. The quantum wells are located at 250 nm from the surface with a 2 nm thick AlN barrier located 20 nm above the quantum wells. More details on the sample can be found in [14].

5.2 Fitting the data: accuracy and precision

Using the InGaN/GaN quantum well heterostructure (see Fig. 6c), we measure the decay trace of the quantum wells at λ = 400 ± 35 nm using the three lifetime modes discussed above. All measurements were done with the same current I = 1.5 pA. For ease of argument we define a dose of electrons as the number of electrons exciting the sample in 10 s (9.4×10^7 electrons). The results are summarized in Fig. 6.

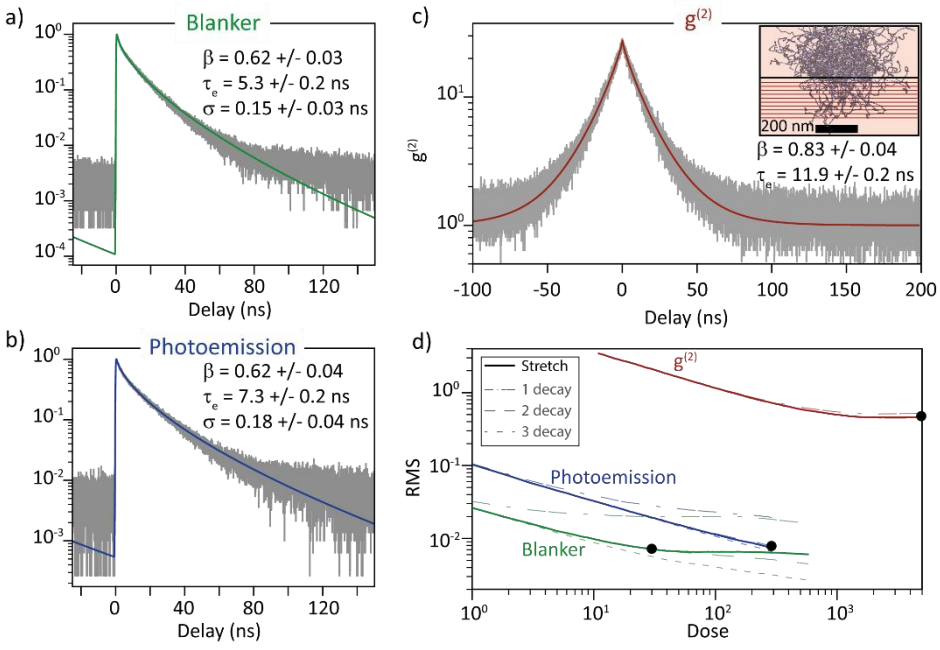

Figure 6: Lifetime measurements of a heterostructure composed of 10 InGaN/GaN quantum wells. The measurements are fitted with a stretched exponential for the three different

configurations at 30 keV and plotted with a log scale. a) ultra-fast blanker, b) laser-driven cathode, and c) autocorrelation measurement using a continuous beam. Fits to the data are shown as drawn lines and the fit parameters are indicated. d) Root mean square of the fit as a function of electron dose (defined as 9.4×10^7 electrons in 10 s of irradiation) for the three configurations. Solid lines represent the RMS for the stretched exponential fits. The faded dashed lines show the RMS for multi-exponential fits with one, two, or three exponentials. The data used for each configuration for a), b), and c) are indicated with dark points. Inset b): Sketch of sample structure used. The pear of interaction is represented in transparent blue and has been calculated using Casino software [37].

In order to compare the level of accuracy and precision that can be reached for each mode, we model the decay traces with a stretched exponential [38].

$$P(t) = \begin{cases} 0 \ \ (t < t_0) \\ e^{-\left(\frac{|t-t_0|}{\tau_e}\right)^{\beta}} \ \ (t > t_0) \end{cases}$$

The decay trace is convolved with a Gaussian function to take into account the IRF of the signal. The modeled function is:

$$f_d(\tau) = e^{-\frac{(t-t_0)^2}{2\sigma^2}} * P(t)$$

Decay traces and fits for the ultra-fast beam blanker and the laser-driven cathode are displayed in Figs. 6a and b, respectively. The standard deviations are σ = 0.13 ns and σ = 0.17 ns, respectively and correspond to a FWHM of 305 ps and 400 ps, which is much larger than the IRF determined in Section 4 with transition radiation decay (σ = 0.06 ns for ultra-fast blanker and σ = 0.03 ns for the photoemission). We attribute the larger value for σ to a delay between excitation and emission caused by diffusion of the electron-beam excited carriers to the emitting centers [39]. Such diffusion dynamics are not revealed by $g^{(2)}$ measurements. The variation of lifetime between the two decays is attributed to the variation within the sample as explained below.

The $g^{(2)}$ data, taken in continuous mode (Fig. 6c), are also modeled with a stretched exponential decay function:

$$f_g(\tau) = 1 + g_e \exp\left(-\left(\frac{|t-t_0|}{\tau_e}\right)^{\beta}\right)$$

Here the data are not convolved with a time-broadened excitation process, as the zero is determined by the symmetry of the curve. From the $g^{(2)}$ measurement we find τ = 11.9 ns and β = 0.83. These numbers are different than for the pulsed measurements in Fig. 6a,b. However, the value of τ_e varies between measurements in a range 5-12 ns, depending mostly on the position but also on the number of electrons per pulse, as well as degradation induced by the electron beam. The lower β found for the pulsed measurements represents a broader range of decay processes in the pulsed excitation process.

Finally, we evaluate the electron dose needed to reach a certain level of precision, given by the root mean square (RMS) of the difference between the data (y_{exp}) and fitted function (y_{fit}). The RMS is calculated for subsequent measurements taken for increasing electron dose for each configuration, and the result is shown in Fig. 6d. The lowest RMS is found for the ultrafast beam blanking and pulsed-laser mode. Both curves show a similar trend with dose, with the photoemission curve shifted by about factor 10 on the horizontal axis. We attribute this shift to the fact that the count rate in this geometry is ~10 times lower (~10^3 versus 10^4 cts/s). This is due to a non-optimal coupling of the CL

light to the optical fiber. For a given dose, the RMS of the $g^{(2)}$ measurement is significantly higher than for the two decay trace acquisitions. It is interesting to note that the stretched exponential does not fully describe the dynamics, especially the very long component visible in both Figure 6a) and b). This long component is due the localization of electrons and holes in separate potential minima [40], [41]. In Figure 6d) the RMS of the ultrafast blanker saturates for a dose superior to 30 while the RMS for a fit with 3 decays continues to improve with the dose. This is a good demonstration that the decay trace is revealing the complex dynamics of the sample while the RMS of the $g^{(2)}$ is similar for multiple exponential decay or a stretched exponential.

We note that for all configurations, for a given time binning of the correlator, a measurement of a smaller lifetime will result in a higher signal-to-noise ratio for the same time of acquisition. Furthermore, the repetition rate of the pulsed electron beam can be increased when shorter lifetimes are measured, increasing the total photon flux while maintaining less than one photon per pulse (to avoid pulse picking). Similarly, a value for $g^{(2)}(0)$ is collected faster for shorter lifetimes, as all photons emitted by a single electron are located in fewer time bins.

Due to the higher signal-to-noise ratio, for a given average beam current the time to acquire a decay trace is much smaller than for a $g^{(2)}$ curve. For example, the $g^{(2)}$ map in Fig. 6c took 14h to collect while the decay trace measurements of Fig. 6a took 5 min. The two curves were taken with the same number of photon counts on the detectors. Decay trace measurements are thus better suited for samples that are sensitive to beam damage and enable faster acquisition of two dimensional lifetime maps. Also, with a faster acquisition time, drift effects can be mitigated, which may result in a higher spatial resolution even if the intrinsic SEM resolution is deteriorated by using a pulsed beam. However, this will depend on the sample and multiple drift corrections can be applied during the acquisition of a single pixel. Indeed, using drift correction we were able to acquire $g^{(2)}$ maps in 4h with pixel size of 30 nm [42].

An example of a lifetime mapping acquisition with the ultrafast blanker configuration is shown in Fig. 7, where an array of GaN nanorods with embedded InGaN quantum wells [43] is investigated. A ‘‘conventional’’ CL map is shown in Fig. 7a with a false-color RGB map, which is constructed by dividing the wavelength range from 400 to 550 nm in blue (400 - 450 nm), green (450 – 500 nm), and red (500 - 550 nm) color channels. The averaged emission spectra over each nanorod show strong differences for different nanorods. Lifetime traces were then acquired with a pixel size of 50×50 nm. The acquisition was done, with V = ±5V, E = 5 keV, and L = 0.25 mm (Δp = 100 ps). The acquisition time per pixel was set to 60 s. To avoid sample drift during acquisition a drift correction was performed every 10 s using the SE images of a specific region. This procedure allows to reposition the beam with respect to the structure during the acquisition. For fitting the decay traces we used a convolution of a 200 ps-FWHM Gaussian representing the IRF, and a double-exponential decay. The lifetime of the main exponential, which constitutes more than 90% of the initial amplitude, is displayed in Fig. 7. It shows distinct variations within each individual nanorod and varies between 300 and 900 ps. The loss of spatial resolution in changing from continuous to pulsed mode is visible in the secondary electron images acquired simultaneously with the lifetime mapping. Nonetheless, the smallest nanorods with a diameter of 200 nm can clearly be resolved.

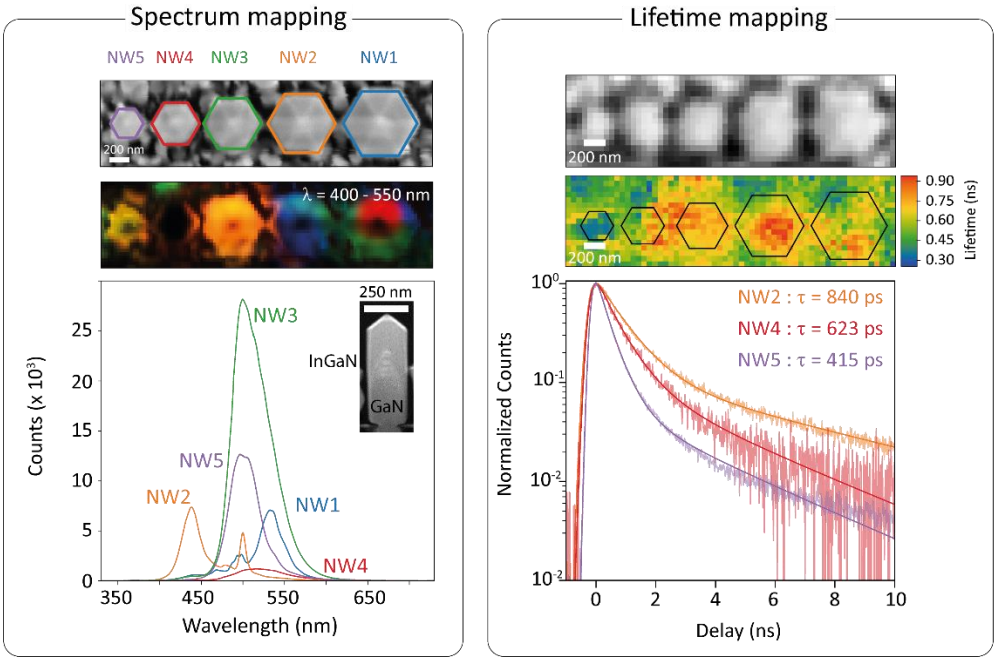

Figure 7 : Cathodoluminescence spectral and lifetime maps for InGaN quantum wells embedded in an array of GaN nanorods (pixel size 50×50 nm). Spectral map: top: SEM image, center: RGB false-color image extracted from the CL data cube. The spectra are separated in 3 sections (blue, green and red, in the range from 400 - 550 nm) which are binned such that the total intensity in these spectral regions defines an RGB code for every position. bottom: average spectrum for each wire. Lifetime map (5 keV, V = ±5V (Δp = ~100 ps)): top: SEM image, center: map of fitted long lifetime decay components, bottom: Average decay trace for select wires.

These measurements show the power of spatially-resolved decay trace acquisition to characterize the dynamics of semiconductor and other materials. Picosecond CL lifetime imaging has been used by Jacopin et al. to image the exciton dynamics near a single dislocation in GaN [44] and by Deveaud et al. to measure the diffusion length of carriers and the non-exponential decay of III-V nanostructures [35]. However, we showed that spatially-resolved measurements of $g^{(2)}(t)$ provide a way to determine the local probability of excitation [14] and disentangle variations in excitation and radiative efficiency in a spatially resolved way [42].

6 Conclusion

In this paper, we discussed the advantages and disadvantages of different cathodoluminescence lifetime measurements and imaging techniques in terms of complexity of implementation, spatial and temporal resolution, and measurement precision. The use of a pulsed electron beam in combination with decay trace measurements allows for the most detailed measurement of the temporal CL dynamics and provides the highest lifetime measurement accuracy. Lifetimes derived from $g^{(2)}$ measurements have lower accuracy but do not require a pulsed beam, and images have a spatial resolution that is only limited by the performance of the microscope. Pulsed $g^{(2)}$ measurements can be used to increase the signal-to-noise ratio. Moreover, they provide an effective method to study single-electron effects on the light emission. The ultrafast blanker configuration enables a broad range of pulse widths and repetition rates. By modifying two apertures in the electron column we obtain pulse widths of 30 ps and 163 ps in conjugate mode at 5 and 30 keV, respectively. However, in the case of the ultra-fast beam blanker the higher time-resolution often

leads to lower spatial resolution and a tradeoff has to be found depending on the experiment. A conjugate plane geometry of the electron column is required to optimize beam blanking, as is the placement of a small aperture of 30 μm after the second condenser to gain in time resolution without losing current in standard configuration. The pulsed-laser driven photoemission geometry delivers the shortest electron pulses, and theoretically a low loss in spatial resolution. In order to take advantage of the picosecond pulses that are generated in the photoemission process, a streak camera [35], [45] or pump-probe configuration [17], [46] are needed. In both pulsed configurations the average number of electrons per pulse can typically be tuned in the range of 1-100. Using a proper model spatial maps of the relative excitation and de-excitation rates of optical emitters can be derived from the $g^{(2)}$ maps. We believe that all time-resolved CL techniques presented here are complementary, with the particular choice of one or the other determined by the requirements in terms of temporal resolution, spatial resolution and acquisition time.

Acknowledgements

This work is part of the research program of the 'Nederlandse organisatie voor Wetenschappelijk Onderzoek' (NWO). It is also funded by the European Research Council (ERC). Y.H.R. and Z.M. thank the support from the Natural Sciences and Engineering Research Council of Canada (NSERC) and National Science Foundation (Grant ECCS-1709207). M.L. and S.C. gratefully acknowledge the German Research Foundation (DFG) for financial support through the cluster of excellence 'Engineering of Advanced Materials' at the Friedrich-Alexander-Universität Erlangen-Nürnberg. We gratefully acknowledge Gerward Weppelman and Jacob Hoogenboom (TU Delft) for useful discussions and advice regarding beam blanking, and technical assistance of Eric Piel, Ronald Buijs and Duncan Verheijde.

Notes: The authors declare the following competing financial interest(s): A.P. is co-founder and co-owner and T.C. is employee of Delmic BV, a company that produces a commercial cathodoluminescence system that was used in this work. E.K. is employee of Thermo Fisher, a company that produces the commercial SEMs used in this work.

Appendix A. Spatial resolution analysis

For characterization of the spatial resolution we acquired SEM images on a tin particle calibration sample under various conditions. There are several ways to establish the spatial resolution of an SEM. Rather than relying on particular user-guided cross cuts through the image, we take a more general approach and use a Fourier transform based method as outlined in [28]. For this method to be valid it is important that the sample has features that are fine enough and that they are homogeneously distributed. In this sample the (quasi) spherical shapes, broad size distribution and sharp high-contrast edges ensure that these conditions are met for these SEMs and imaging conditions.

The images acquired in the SEM have a 3:4 aspect ratio from which we extract two distinct square images (with some overlap in the middle) to improve the fidelity of the analysis. One such image taken in continuous mode at 30 kV is shown in Fig. S1 (a). From this image we calculate the 2D power spectrum by calculating the Fourier transform of the image using a fast Fourier transform algorithm and multiplying that with its complex conjugate. To prevent artifacts due to the image edge in the 2D power spectrum, the image data is multiplied with a radial von Hann filter window: $\frac{1}{2}\left(1-\cos\left(\frac{2\pi r}{N-1}\right)\right)$

where $r = \sqrt{n_x^2 + n_y^2}$ is the radial distance from the center in pixels and *N* is the total number of pixels in the image. The resulting 2D power spectrum is shown in Fig. S1 (b). Subsequently, we establish the highest spatial frequency present in the image data which corresponds to the smallest distance which can be resolved by microscope. This frequency is found where the central peak in the power spectrum (representing the tin particle data in the image) becomes flat and merges with the noise in the image. To find this point we threshold the data using the gradient of the radially averaged power spectrum. The radially averaged power spectrum is shown in Fig. S1 (c) together with the found resolution threshold. This threshold is also indicated in Fig. S1 (b) as a white dashed circle. Although this approach presents an effective method we have to take one further precaution. Vibrations present in the SEM image manifest themselves as additional features in the power spectrum unrelated to the sample features. These often occur at high spatial frequencies as these modulations are present from scan line to scan line and interfere with establishing the correct threshold. We removed these contributions by omitting the angular wedges in between the blue dashed lines (see Figure S1 (b)) from the radial average.

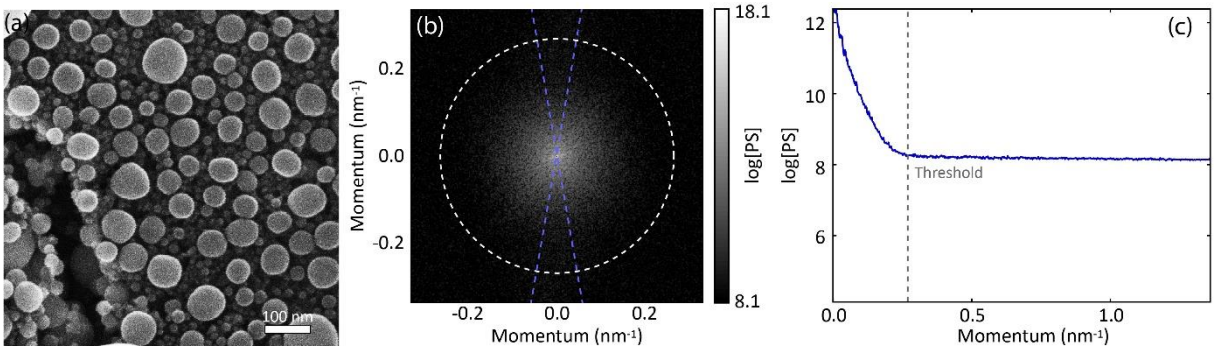

Figure A1: (a) SEM image acquired at 30 kV (≈ 200 pA) with a continuous beam in normal imaging mode. (b) 2D power spectrum derived from (a) plotted with a logarithmic color scale. The retrieved highest spatial frequency/resolution is indicated by the white dashed circle. The blue dashed lines indicate which parts of the power spectrum are omitted from the radial average to prevent artifacts from the vibrations. (c) Radially averaged power spectrum as function of momentum. The threshold indicating the highest spatial frequency present in the image is shown by the gray dashed line (~4 nm in this case).

We note that the average resolution reported here, neglects any potential asymmetries in the electron beam focusing. Indeed, in some of the images the power spectrum is clearly elliptical in shape indicating that the spatial resolution is non-isotropic. This could be due to astigmatism in the beam or to other distortions that are induced by the beam alignment/blanking. Due to the lower current, the SEM images that are taken under pulsed conditions have a significantly lower signal-to-noise ratio than the images acquired in continuous mode giving a larger error in establishing the threshold. Taking this into account, we estimate the relative error to be ~10-20% for the continuous images and ~20-30% for the pulsed images.

References

[1] T. Coenen and N. M. Haegel, 'Cathodoluminescence for the 21st century: Learning more from light', *Appl. Phys. Rev.*, vol. 4, no. 3, p. 031103, 2017.

[2] M. Merano *et al.*, 'Probing carrier dynamics in nanostructures by picosecond

cathodoluminescence.', *Nature*, vol. 438, no. 7067, pp. 479–82, Nov. 2005.

[3] S. Sonderegger *et al.*, 'High spatial resolution picosecond cathodoluminescence of InGaN quantum wells', *Appl. Phys. Lett.*, vol. 89, no. 23, p. 232109, 2006.

[4] R. J. Moerland, I. G. C. Weppelman, M. W. H. Garming, P. Kruit, and J. P. Hoogenboom, 'Time-resolved cathodoluminescence microscopy with sub-nanosecond beam blanking for direct evaluation of the local density of states', *Opt. Express*, vol. 24, no. 21, p. 24760, 2016.

[5] S. Meuret *et al.*, 'Lifetime Measurements Well below the Optical Diffraction Limit', *ACS Photonics*, vol. 3, no. 7, pp. 1157–1163, 2016.

[6] H. Lourenço-Martins *et al.*, 'Probing Plasmon-NV 0 Coupling at the Nanometer Scale with Photons and Fast Electrons', *ACS Photonics*, 2017.

[7] A. Bell *et al.*, 'Localization versus field effects in single InGaN quantum wells Localization versus field effects in single InGaN quantum wells', vol. 58, pp. 1–4, 2004.

[8] M. A. Herman, D. Bimberg, and J. Christen, 'Heterointerfaces in quantum wells and epitaxial growth processes: Evaluation by luminescence techniques', *J. Appl. Phys.*, vol. 70, no. 2, 1991.

[9] F. Carbone, B. Barwick, O.-H. Kwon, H. S. Park, J. Spencer Baskin, and A. H. Zewail, 'EELS femtosecond resolved in 4D ultrafast electron microscopy', *Chem. Phys. Lett.*, vol. 468, no. 4–6, pp. 107–111, Jan. 2009.

[10] D. Yang, O. F. Mohammed, and A. H. Zewail, 'Scanning ultrafast electron microscopy', vol. 2010, 2010.

[11] A. Feist, K. E. Echternkamp, J. Schauss, S. V. Yalunin, S. Sch??fer, and C. Ropers, 'Quantum coherent optical phase modulation in an ultrafast transmission electron microscope', *Nature*, vol. 521, no. 7551, pp. 200–203, 2015.

[12] A. Feist *et al.*, 'Ultrafast transmission electron microscopy using a laser-driven field emitter: Femtosecond resolution with a high coherence electron beam', *Ultramicroscopy*, vol. 176, no. October 2016, pp. 63–73, 2017.

[13] T. Onuma *et al.*, 'measurement of GaN cathodoluminescence measurement of GaN', vol. 043905, 2012.

[14] S. Meuret *et al.*, 'Photon bunching reveals single-electron cathodoluminescence excitation efficiency in InGaN quantum wells', *Phys. Rev. B*, vol. 96, no. 3, pp. 1–8, 2017.

[15] G. S. Plows and W. C. Nixon, 'Stroboscopic scanning electron microscopy', *J. Phys. E.*, vol. 1, no. 6, p. 595, 1968.

[16] A. H. Zewail, 'Four-Dimensional Electron Microscopy', *Science (80-.).*, vol. 328, no. 5975, pp. 187–193, 2010.

[17] J. Sun, A. Adhikari, B. S. Shaheen, H. Yang, and O. F. Mohammed, 'Mapping Carrier Dynamics on Material Surfaces in Space and Time using Scanning Ultrafast Electron Microscopy', *J. Phys. Chem. Lett.*, vol. 7, no. 6, pp. 985–994, 2016.

[18] P. Hommelhoff, Y. Sortais, A. Aghajani-Talesh, and M. A. Kasevich, 'Field emission tip as a nanometer source of free electron femtosecond pulses', *Phys. Rev. Lett.*, vol. 96, no. 7, pp. 1–4, 2006.

[19] F. Houdellier, G. M. Caruso, S. Weber, M. Kociak, and A. Arbouet, 'Development of a high brightness ultrafast Transmission Electron Microscope based on a laser-driven cold field emission source', *Ultramicroscopy*, vol. 186, pp. 128–138, 2018.

[20] R.F. Egerton, *EELS in the Electron Microscope*. 1996.

[21] R. Hanbury Brown and R. Q. Twiss, 'Correlation between photons in two coherent beams of light', *J. Astrophys. Astron.*, vol. 15, no. 1, pp. 13–19, Mar. 1994.

[22] C. Santori, M. Pelton, G. Solomon, Y. Dale, and Y. Yamamoto, 'Triggered Single Photons from a Quantum Dot', *Phys. Rev. Lett.*, vol. 86, no. 8, pp. 1502–1505, Feb. 2001.

[23] R. Alléaume, F. Treussart, J.-M. Courty, and J.-F. Roch, 'Photon statistics characterization of a single-photon source', *New J. Phys.*, vol. 6, no. 04, pp. 85–85, Jul. 2004.

[24] a. Lebreton, I. Abram, R. Braive, I. Sagnes, I. Robert-Philip, and a. Beveratos, 'Unequivocal Differentiation of Coherent and Chaotic Light through Interferometric Photon Correlation Measurements', *Phys. Rev. Lett.*, vol. 110, no. 16, p. 163603, Apr. 2013.

[25] T. Jeltes *et al.*, 'Comparison of the Hanbury Brown-Twiss effect for bosons and fermions.', *Nature*, vol. 445, no. 7126, pp. 402–5, Jan. 2007.

[26] S. Meuret *et al.*, 'Photon Bunching in Cathodoluminescence', *Phys. Rev. Lett.*, vol. 114, no. 19, pp. 1–5, 2015.

[27] L. Novotny and B. Hecht, *Principles of Nano-Optics*. 2006.

[28] D. C. Joy, Y.-U. Ko, and J. J. Hwu, 'Metrics of resolution and performance for CD-SEMs', *Proc. SPIE*, 2000.

[29] B. G. Yacobi and D. B. Holt, *Cathodoluminescence Microscopy of Inorganic Solids*. New York: Springer, 1990.

[30] W. Knauer, 'Boersch effect in electronoptical instruments', vol. 1676, no. 1979, 2014.

[31] W. Qian, M. R. Scheinfein, and J. C. H. Spence, 'Brightness measurements of nanometer-sized field-emission-electron sources', *J. Appl. Phys.*, vol. 73, no. 11, pp. 7041–7045, 1993.

[32] M. Kuwahara *et al.*, 'The Boersch effect in a picosecond pulsed electron beam emitted from a semiconductor photocathode', *Appl. Phys. Lett.*, vol. 109, no. 1, 2016.

[33] B. J. M. Brenny, A. Polman, and F. J. García De Abajo, 'Femtosecond plasmon and photon wave packets excited by a high-energy electron on a metal or dielectric surface', *Phys. Rev. B*, vol. 94, no. 15, pp. 1–11, 2016.

[34] A. Adhikari, J. K. Eliason, J. Sun, R. Bose, D. J. Flannigan, and O. F. Mohammed, 'Four-Dimensional Ultrafast Electron Microscopy: Insights into an Emerging Technique', *ACS Appl. Mater. Interfaces*, vol. 9, no. 1, pp. 3–16, 2017.

[35] P. Corfdir *et al.*, 'Exciton recombination dynamics in a-plane (Al,Ga)N/GaN quantum wells probed by picosecond photo and cathodoluminescence', *J. Appl. Phys.*, vol. 107, no. 4, p. 43524, 2010.

[36] P. Kapusta, M. Wahl, and R. Erdmann, Eds., *Advanced Photon Counting*. Springer International Publishing, 2015.

[37] H. Demers *et al.*, 'Three-dimensional electron microscopy simulation with the CASINO Monte Carlo software', *Scanning*, vol. 33, no. 3, pp. 135–146, 2011.

[38] K. C. B. Lee *et al.*, 'Application of the Stretched Exponential Function to Fluorescence Lifetime Imaging', *Biophys. J.*, vol. 81, no. 3, pp. 1265–1274, 2001.

[39] Z. Z. Bandić, P. M. Bridger, E. C. Piquette, and T. C. McGill, 'Electron diffusion length and

lifetime in p-type GaN', *Appl. Phys. Lett.*, vol. 73, no. 22, pp. 3276–3278, 1998.

[40] F. Feix *et al.*, 'Ga-Polar (In,Ga) N/GaN Quantum Wells Versus N-Polar (In,Ga)N Quantum Disks in GaN Nanowires: A Comparative Analysis of Carrier Recombination, Diffusion, and Radiative Efficiency', *Phys. Rev. Appl.*, vol. 8, no. 1, pp. 1–13, 2017.

[41] C.-N. Brosseau, M. Perrin, C. Silva, and R. Leonelli, 'Carrier recombination dynamics in <math display="inline"> <mrow> <msub> <mrow> <mtext>In</mtext> </mrow> <mi>x</mi> </msub> <msub> <mrow> <mtext>Ga</mtext> </mrow> <mrow> <mn>1</mn> <mo>−</mo> <mi>x</mi> </mrow> </msub> <mtext>N</mtext> <mo>/</mo> <mtext>', *Phys. Rev. B*, vol. 82, no. 8, p. 085305, 2010.

[42] S. Meuret, T. Coenen, S. Y. Woo, Y. H. Ra, Z. Mi, and A. Polman, 'Nanoscale Relative Emission Efficiency Mapping Using Cathodoluminescence g(2)Imaging', *Nano Lett.*, vol. 18, no. 4, pp. 2288–2293, 2018.

[43] Y. H. Ra *et al.*, 'Full-color single nanowire pixels for projection displays', *Nano Lett.*, vol. 16, no. 7, pp. 4608–4615, 2016.

[44] W. Liu, J. F. Carlin, N. Grandjean, B. Deveaud, and G. Jacopin, 'Exciton dynamics at a single dislocation in GaN probed by picosecond time-resolved cathodoluminescence', *Appl. Phys. Lett.*, vol. 109, no. 4, 2016.

[45] M. Tchernycheva *et al.*, 'Core–shell InGaN/GaN nanowire light emitting diodes analyzed by electron beam induced current microscopy and cathodoluminescence mapping', *Nanoscale*, vol. 7, no. 27, pp. 11692–11701, 2015.

[46] T. Eggebrecht *et al.*, 'Light-Induced Metastable Magnetic Texture Uncovered by in situ Lorentz Microscopy', *Phys. Rev. Lett.*, vol. 118, no. 9, pp. 1–7, 2017.